Enhanced dispersion in shear-thinning fluid flow through porous media

Amna Al-Qenae
Department of Chemical Engineering, The University of Manchester, Manchester M13 9PL, United Kingdom and Kuwait Oil Company, Ahmadi 9758, Kuwait

Javad Shokri
Department of Chemical Engineering, The University of Manchester, Manchester M13 9PL, United Kingdom

Takshak Shende
Department of Mechanical Engineering, University College London, United Kingdom

Muhammad Sahimi
Mork Family Department of Chemical Engineering and Materials Science, University of Southern California, USA

Vahid Niasar*
Department of Chemical Engineering, The University of Manchester, Manchester M13 9PL, United Kingdom

(Received 1 November 2024; accepted 19 May 2025; published 25 June 2025)

Mixing and dispersion in random porous materials are complex processes governed by the interplay of local velocity fields and pore morphology randomness. For purely advective transport in Newtonian fluid flow within porous media at macro scale, a linear relationship is established between the dispersion coefficient and average interstitial velocity, characterized by a coefficient known as dispersivity. Previous studies highlight that dispersivity remains constant and is solely dependent on the properties of the porous medium. However, whether dispersivity is constant when considering non-Newtonian fluids, which exhibit spatially variable viscosity, is questionable. For example, for a shear-thinning fluid, viscosity decreases as the shear rate increases. In non-Newtonian shear-thinning fluids, viscosity varies across pore spaces, influenced by local shear rates, making pore size distribution and fluid pathway connectivity critical factors that impact solute transport dynamics. In this study, we present experimental insights into solute transport for both non-Newtonian and Newtonian fluid flows within porous media using glass micromodels and optical microscopy. Xanthan gum solution, representing a shear-thinning fluid, and water, as a Newtonian control, were used to evaluate the differences in transport behavior. Results indicate an enhanced dispersion effect for shear-thinning fluids in porous media. While dispersivity remains constant in Newtonian fluid flow, our experiments reveal a nonmonotonic relationship between dispersivity and injection rate for shear-thinning fluids. Unlike in Newtonian fluids, dispersivity in non-Newtonian fluids is influenced not only by the properties of the porous medium but also by the fluid's rheology. We propose a mathematical model to account for this variability, offering a framework that aligns with

*Contact author: vahid.niasar@manchester.ac.uk

Published by the American Physical Society under the terms of the Creative Commons Attribution 4.0 International license. Further distribution of this work must maintain attribution to the author(s) and the published article's title, journal citation, and DOI.

our experimental findings and provides insights into the mechanisms governing solute transport in non-Newtonian fluid flow within porous media.

DOI: 10.1103/5m8s-g4zy

I. INTRODUCTION

Non-Newtonian fluids [1] have numerous applications in a variety of disciplines, ranging from food processing [2] and drug delivery [3,4], to groundwater remediation [5] and hydrocarbon recovery [6]. In particular, flow of non-Newtonian fluids through heterogeneous porous media has been of considerable interest for quite some time [7]. Our focus in the present paper is on shear-thinning fluids. In contrast to Newtonian fluids, the nonlinear relationship between the shear stress and shear rate in such fluids, characterized by viscosity reduction at higher shear rates [8], complicates modeling and predicting flow and transport processes in porous media.

An important related problem is solute transport in flow of non-Newtonian fluids through a porous medium. Although dispersion in flow of Newtonian fluids has been extensively studied [9–11], the literature on solute transport in non-Newtonian fluid flow in porous media is relatively scant. Furthermore, upscaling of transport in porous media when non-Newtonian fluids are involved is not fully understood yet [9,12], since the local viscosity varies spatially. The complexity arises from the interplay between the fluid's rheology and the heterogeneous morphology of porous media, which gives rise to a rich variety of phenomena. Similar to Newtonian fluids, non-Newtonian fluids influence solute transport in porous media through the fluid velocity distribution [13], which in turns depends on the morphology of the pore space. A shear-thinning fluid behaves similarly to a Newtonian one at very low or very high shear rates, where the change in the effective viscosity with shear rate can be neglected. In the middle of the range of shear rates, however, notable viscosity changes affect the velocity distribution significantly, leading to a much broader distribution of pore-scale transport times and stronger dispersion [14,15] of a solute. The purpose of the present paper is to report on the results of an extensive experimental study of solute transport in flow of shear-thinning fluids in porous media, in the range of shear rates that cause significant viscosity variations.

Non-Newtonian fluid flow and transport in porous media have been studied previously using pore-scale modeling [9,15–18] and non-Newtonian fluid flow using pore-scale experiments [19]. At the Darcy scale, the dispersion results from a velocity streamline difference caused by permeability heterogeneity [10]. However, at the pore scale, the velocity streamline difference is because of the variation in pore shapes and sizes. Browne *et al.* [20] reviewed how properties of polymer solutions influence their flow in microfluidic systems. The dynamics of flow of polymer solutions in porous media exhibit nontrivial patterns, and is influenced by a combination of polymer conformations, flow conditions, and the morphology of the pore space. As is well known, solute transport in porous media is driven by two mechanisms. One is kinematic, since in a pore space stream-tubes branch out and rejoin repeatedly at the junctions of flow passages. The resulting tangling and divergence of streamlines is strengthened by the widely varying orientations of flow passages and the local connectivity of the pore space, giving rise to wide variations in the lengths of the streamlines and their downstream separations. The second mechanism is dynamic, because the speed by which a solute tracer is transported along a given flow passage depends on the flow resistance or hydraulic conductance of the passage, its orientation, and the local pressure field. The two mechanisms also govern solute transport in flow of non-Newtonian fluids in porous media, with the added complexities arising from the rheology of the fluid and its interaction with the morphology of the pore space, which imposes both shear and extension, hence elongating polymers.

Paterson *et al.* [21] carried out an experimental study on the dispersion of tracers in flow of a shear-thinning polymer solution in a granular porous medium. The effect of the concentration of the polymer and of the flow rate was investigated. The experiments indicated that, compared with Newtonian fluids at an identical effective Péclet numbers, normalized dispersivity of a tracer in

non-Newtonian fluids, a measure of how far the solute spreads out in a porous medium, significantly increases. Péclet number (*Pe*), the ratio of advection and diffusion rates, was related to the shear-thinning properties of the non-Newtonian fluids. D'Onofrio *et al.* [22] carried out tracer dispersion measurements at various flow rates using shear-thinning polymers in a double porosity model, i.e., one with two distinct family of transport paths [23,24]. The goal of the study was investigating the influence of the nonlinearity in the shear rate-shear stress relationship on solute transport. It was found that, increasing the polymer concentration increased the strength of the nonlinearity, and gave rise to higher dispersivities. Browne *et al.* [25] studied the impact of elastic turbulence on transport through porous media with stratified structures. Their experiments revealed that adding polymers to the fluids can effectively achieve homogenized fluid front across the strata with permeability contrast, which has important implications for improving the efficiency of transport in various processes involving porous media.

Theoretically, Dejam [26] studied solute dispersion in flow of a power-law fluid in a conduit with porous walls. The study developed a reduced-order model to determine the dispersion coefficient, governed by both the *Pe* and a "flow behavior index" that characterized the extent of the deviation of the behavior of a fluid from Newtonian rheology. The dispersion coefficients for shear-thinning fluids were found to be smaller than those for Newtonian ones, whereas those for shear-thickening fluids were relatively higher. It was also shown that, at a given *Pe*, the dimensionless dispersion coefficient—the ratio of the dispersion coefficient solely due to advection, and the diffusion coefficient—increased in fluids with a higher power-law index, and that at higher flow behavior index, the possibility of early solute breakthrough in the porous conduit increased.

There is a significant gap in understanding the dependence of the transport of a solute on the rheology of a non-Newtonian fluid as well as dispersivity for non-Newtonian fluids. The objective of the present study is to report on an extensive experimental study of the effect of the *Pe* on solute transport in porous media, employing both Newtonian and non-Newtonian shear-thinning fluids. Our goal is to understand how the dispersivity is influenced by non-Newtonian fluid rheology using an experimental setup involved a microfluidic chip representing a porous medium.

The experimental setup involved a microfluidic chip representing a porous medium. Various fluids were injected at different flow rates to comprehend the impact of fluid velocity/*Pe* on dispersion in the porous medium, comparing Newtonian and non-Newtonian fluids. Through the analysis of time-elapsed optical images of concentration fields in the micromodel, breakthrough concentration profiles were calculated. As a postprocessing step, the dispersion coefficient, dispersivity, and fractal dimension of the concentration fields were determined.

II. MATERIALS AND METHODS

We first describe the preparation of the fluids and measurement of the rheological properties of interest to us, followed by the description of the experimental system and the procedure for making the measurements.

A. Fluids preparation and rheology measurement

We employed four solutions in the fluid flow problem. Two of them were Newtonian, while the other two represented non-Newtonian shear-thinning fluids. The solutions included (i) clear deionized water (clear DI), (ii) deionized water mixed with ink (Ecoline, water-based blue color) at a 50% mass concentration (dyed DI), (iii) clear Xanthan gum solution (clear XG, 0.05% XG mass concentration), and (iv) dyed Xanthan gum solution (dyed XG, 0.05% XG mass concentration). Xanthan gum, a biopolymer, was chosen as the non-Newtonian fluid due to its ease of use in the laboratory and its common use in previous studies [27]. The shear-thinning solutions were prepared by mixing the Xanthan gum (XG) powder in deionized water using an overhead mixer for ten minutes. Subsequently, a buchner funnel filtration process was carried out twice, employing two filtration papers (Fisherbrand™, Grade 601), which was aimed at removing any remaining

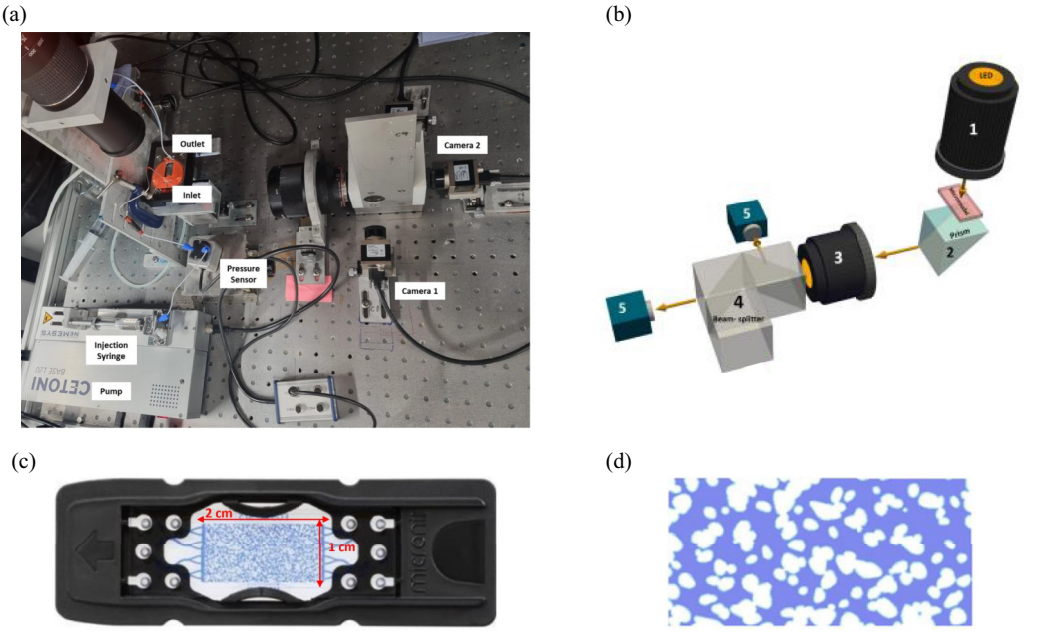


FIG. 1. The micromodel experimental setup, (a) the micromodel flow experimental setup and visualization system, (b) a schematic representation of the experimental setup [29] including (1) collimated LED light source, (2) beam-splitter, (3) magnifying lens, (4) beam-splitter box, (5) 12-megapixel monochrome cameras, (c) the transparent micromodel, which is quasi-3D porous medium, (d) a magnified part of the Micronit^{TM} micromodel.

undissolved aggregates, ensuring the elimination of potential blockages in the microfluidic chip. The bulk rheology of clear and dyed XG solutions were measured using an Anton-Paar device (Modular Compact Rheometer MCR 92) with the DG42 module that measures the viscosity as a function of the shear rates, from 1 to 1000 s^{-1}. The rheological measurements were carried out in triplicate to ensure the consistency and accuracy of the data.

B. Experimental setup and procedure

The experimental setup, as illustrated in Fig. 1(a), was similar to the one introduced in former studies as previously described in detail [28,29]. A transparent glass microfluidic chip (Micronit^{TM}) (enhanced oil recovery glass chip) with resembling sandstone pore morphology as shown in Fig. 1(b), with a depth of 20 μm and an average pore radius of 75 μm, was utilized. A precision pump (Cetoni, Nemesys midpressure module) was employed for fluid injection, with the inlet pressure monitored by a pressure sensor (maximum pressure of 2 bar). Fluid transport in the microfluidic chip was recorded at varying frame rates, depending on the injection rate, using a custom optical system comprising a right-angle prism, a magnifying lens, three beam splitters, and two 12-megapixel monochrome cameras (BASLER acA4112-30um).

To ensure consistent initial conditions for the experiments, the permeability of the microfluidic chip was measured before each experiment. This involved injecting DI water into the micromodel at various flow rates and measuring the resulting pressure drop. For both Newtonian and non-Newtonian fluids, the microfluidic chip was initially saturated with the clear solution. Subsequently, the loading cycle commenced, where the dyed solution was injected at a constant flow rate, and the concentration map was recorded using the optical system. Four flow rates were selected for the experiments, which were 2×10^{-3}, 2×10^{-4}, 2×10^{-5}, and 2×10^{-6}, all in ml s^{-1}. The values of *Pe* corresponding to the selected injection flow rate are: 3000, 300, 30, and 3. In this study, the

pore-scale Péclet number ($Pe = uL/D_m$) has been used, where L is the characteristic length, the mean pore diameter equal to 0.00015 m. D_m denotes the diffusion coefficient, equal to 10^{-9} m^2 s^{-1} [15]. The calculated Weissenberg numbers (Wi), defining the relative magnitude of elastic stresses to viscous stresses, were 62 for the highest injection flow rate, and 6.2, 0.62, and 0.063 for the lowest flow rates, respectively. Wi was calculated using $Wi = u\lambda/L$, where λ is the relaxation time which is equal to 0.47 (s). While polymeric solutions display a spectrum of stress relaxation times dependent on shear rate [30], we adopted the longest stress relaxation time in our study, aligning with previous research [20,25]. The velocity was converted to shear rate using $\dot{\gamma} = u/L$. These experiments were conducted 1–3 times to ensure the reproducibility of the results.

C. Image processing

The entire length of the microfluidic chip, which was 1 cm × 2 cm, was captured using two cameras, each with a field of view covering about 70% of the length of the porous medium. Due to the large coverage of each camera, all the analysis was performed only on the recorded images from camera one, which covered the inlet of the microfluidic chip. Image processing and data analysis followed the method reported by Karadimitriou *et al.* [31], implemented through a custom MATLAB script. In each image of the time series, the grey-scale intensity of each pixel (I_i) was converted to a dimensionless concentration of that pixel (C_i), ranging from 0 to 1, as follows:

$$C_i = \frac{I_i - I_i^{\text{start}}}{I_i^{\text{end}} - I_i^{\text{start}}}, \tag{1}$$

where I_i^{start} and I_i^{end} denote, respectively, the gray-scale intensity of pixel i at the start and the end of the experiment. The average resident concentration $\bar{C}_t$ at time t is then calculated by computing the arithmetic average of the values of C_i.

D. Upscaling transport properties

The hydrodynamic dispersion coefficient, D [m^2 s^{-1}], was determined using two different methods; fitting an analytical equation to the breakthrough curves and using method of moments to calculate dispersion coefficient.

1. Fitting an analytical equation

The breakthrough curves represent the dynamic evolution of the average effluent concentration at the outlet stripe (100-pixel width of the outlet) versus time. The resulted data were fitted to the Ogata-Banks analytical equation, Eq. (2) [32]. The Ogata-Banks equation was derived for the one-dimensional advection-dispersion equation with the Dirichlet boundary condition, $C(0, t) = C_0$ at the inlet, and the Neumann boundary condition at the outlet, $\partial C(\infty, t)/\partial x = 0$. The pore velocity u and the dispersion coefficient D were fitted to the outlet breakthrough curves:

$$C(x, t) = \frac{1}{2} C_0 \left[\operatorname{erfc}\left(\frac{x - ut}{2\sqrt{Dt}} \right) + \exp\left(\frac{ux}{D} \right) \operatorname{erfc}\left(\frac{x + ut}{2\sqrt{Dt}} \right) \right]. \tag{2}$$

2. Method of moments

The hydrodynamic dispersion coefficient was also calculated using the method of moments (MoM) which has been widely used for advection-dispersion problems in porous media [33–36]. We estimated the hydrodynamic dispersion coefficients based on the moments of the concentration fields based on a time-dependent equation, where the dispersion coefficient is measured with respect to the center of mass with respect to time [33,36–38]. The first moment was linked to the concentration distribution, representing the mean breakthrough time M_1 [38]:

$$M_1 = \sum t \cdot dc, \tag{3}$$

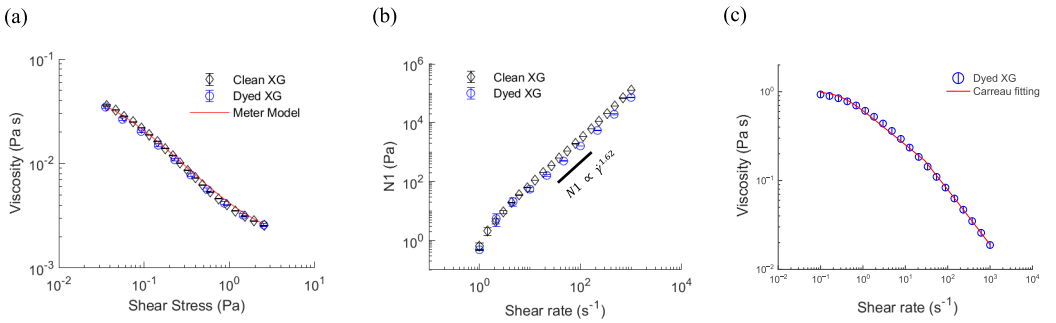


FIG. 2. (a) Rheological data for clear and dyed XG solutions, and their fit to the meter model, Eq. (6). The fitted parameters are $\eta_0 = 0.05587\,\text{Pa s}$, $\eta_\infty = 0.00164\,\text{Pa s}$, $\tau_m = 0.0602\,\text{Pa}$, and $S = 1.0738$. (b) The first normal stress difference for the clear and dyed XG solutions. The error bar shows 95% confidence interval. (c) The Carreau equation fitting for dyes XG, where the viscosity was calculated using $\tilde{\eta} = \frac{\eta - \eta_\infty}{\eta_0 - \eta_\infty}$. The fitted parameter is $n = 0.61$.

where t represents time, and dc represents the concentration. In contrast, the second moment was related to the spread of the concentration profile, represented by the variance of the solute travel time M_2 [38]:

$$M_2 = \sum (t - M_1)^2 \cdot dc, \tag{4}$$

and consequently, pore velocity and dispersion coefficient [38] were calculated as

$$u = \frac{L}{M_1}, \quad D = \frac{M_2 \cdot u^3}{2 \cdot L}, \tag{5}$$

where L represents the length of the system at the outlet stripe, u represents the pore velocity, and D represents the dispersion coefficient.

III. RESULTS AND DISCUSSION

Extensive experiments were carried out in order to study the effect of the various factors on solute transport. In what follows, we present the results and discuss their implications.

A. Bulk rheology

The viscosity-shear measurements were done for both solutions, the clear solution and the dyed one. Adding dye to the solutions makes it act as a tracer. This will help in giving insights about the direction and velocity of the fluid flow, how the fluid interacts with the porous medium, and how the fluid transport is changing in the porous medium due to the fluid-phase occupancy [15,31]. Figure 2(a) displays the evolution of the viscosity with shear stress, for both clear and dyed XG solutions. The results are in agreement with the previously reported data on the rheology of Xanthan gum at a low shear rate at the same temperature and concentration [2,39,40]. Measuring viscosity at shear rates below 10^{-1} s^{-1} was impractical due to the limitations of the rheometer apparatus. The addition of ink to the dyed solution did not alter the rheological characteristics of these solutions. This consistency ensured that the inclusion of ink does not introduce uncertainty in the flow experiments. The viscosity-shear stress experimental data was fitted using the meter model (MM) [41,42], described as

$$\eta_{(\tau)} = \eta_\infty + \frac{\eta_0 - \eta_\infty}{1 + \left(\frac{\tau}{\tau_m}\right)^S}, \tag{6}$$

where τ is the shear stress (Pa), η_0 denotes the viscosity at zero shear stress (Pa s), η_∞ is the viscosity at the infinite shear stress (Pa s), S is the stress-dependent exponent, and τ_m is the shear stress (Pa) when the viscosity of the solution dropped to $(\eta_0 + \eta_\infty)/2$. Figure 2(a) displays an excellent fit of the experimental data by the meter model. Figure 2(b) displays the first normal stress difference (N1) for the clear and dyed XG solutions. The first normal stress difference increases with an increase in shear rate and shows a nonlinear relationship $N1 \propto \dot{\gamma}^{1.62}$. Xanthan gum is a rigid polymer primarily recognized for its remarkable shear-thinning property despite possessing a distinctively measurable value of N1. The first normal stress difference (N1) was measured using the Lodge-Meissner methods [43] available in the Anton-Paar device software. For bulk rheology, various correlation relations have been proposed. We employed the Carreau fluid model [1] to describe the relationship between viscosity, η, and shear rate, $\dot{\gamma}$:

$$\tilde{\eta} = \frac{\eta - \eta_\infty}{\eta_0 - \eta_\infty} = (1 + (\lambda\dot{\gamma})^2)^{(n-1)/2}. \tag{7}$$

The fitted curve has been shown in Fig. 2(c).

B. Solute transport in porous medium

1. Concentration field

Figure 3 depicts the resident concentration map for both Newtonian (DI water) and non-Newtonian (XG) fluids at four different injection rates. The concentration maps are shown at two different times, namely, (i) at an average resident concentration of 0.2, and (ii) at the breakthrough time. Non-Newtonian fluids, known for their viscosity variations in response to shear rate, exhibit a notably faster solute breakthrough, when compared with the Newtonian fluids. The solute breakthrough in the present study was defined as the point when the average outlet solute concentration was equal to 0.03. This specific value was selected for its effectiveness in identifying the fluids' fingering first movement toward the outlet region for most of the injected flow rates. As shown in Fig. 3, the fingering increases with increasing flow rate. Moreover, the fingering breakthrough in the non-Newtonian fluids occurs earlier than in the Newtonian fluids for the intermediate flow rates. Interestingly, with increasing flow rate, the differences between the concentration fields of Xanthan gum and DI water fluids decreases.

2. Breakthrough curves and dispersion coefficients

Figure 4 presents the dynamic evolution of the effluent concentration profiles, as well as their fits using Eq. (2). The profiles are for both the Newtonian and non-Newtonian fluids for four injection rates. The results illustrate that the transport phenomena in the lowest flow rate take the longest time to fully disperse in the porous medium. It is worth noting that the dispersion coefficient fitting for the non-Newtonian cases was better than the Newtonian cases, indicating a good dispersion in the porous media. The fitting accuracy for the non-Newtonian fluid was affected due to the sharp front effect of the Newtonian fluid in the porous medium. Figure 5(a) compares data for the dispersion coefficient, obtained from the experiments with the DI water and XG at various *Pe*, using the Ogata-Banks analytical equation, Eq. (2) [32], which was derived for the steady and uniform flow. To assess whether this assumption influenced the conclusions and the differences in the hydrodynamic dispersion coefficients observed between the Newtonian and non-Newtonian fluids, further analysis using the method of moments was carried out. Also, to increase the reliability of the data, some of the experiments for the Newtonian and non-Newtonian fluids were repeated between 1–3 times at different flow rates.

What stands out in Fig. 5(a) is the general patterns of variations of the dispersion coefficient D_L in the Newtonian and non-Newtonian fluids. The results indicate that the solute in the non-Newtonian fluids has a larger dispersion coefficient than in the Newtonian ones. The data are consistent with D'Onofrio *et al.* [14], as are the trends for solute transport in the non-Newtonian fluid [15], namely, as the flow rate (and, therefore, *Pe*) increases, the velocity of the fluid and the shear rate both

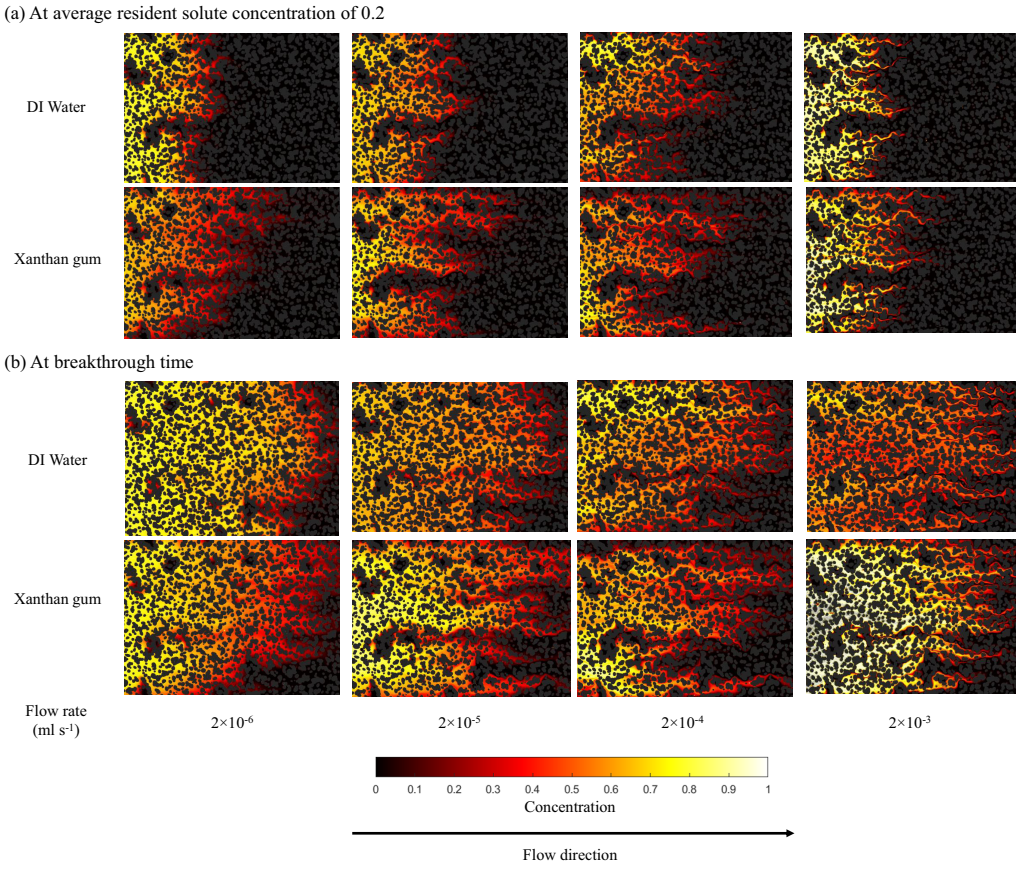


FIG. 3. Concentration maps of the solute in the DI water and XG at various injection rates: (a) at average resident solute concentration of 0.2, and (b) at breakthrough time.

increase, which, in return, contribute to reducing the viscosity of the fluid. At very high Péclet numbers, the non-Newtonian fluid begins to act as a Newtonian one, due to the viscosity-shear rate relationship that becomes flat and much smaller spatial variability of the viscosity. These are also consistent with the experimental data, as at very high flow rates, the dispersion coefficients in the non-Newtonian and Newtonian fluids are essentially the same, as seen in Fig. 5(a). Based on numerous studies and extensive experimental data, the empirical correlation, $D_L = \alpha v^{\beta}$, or,

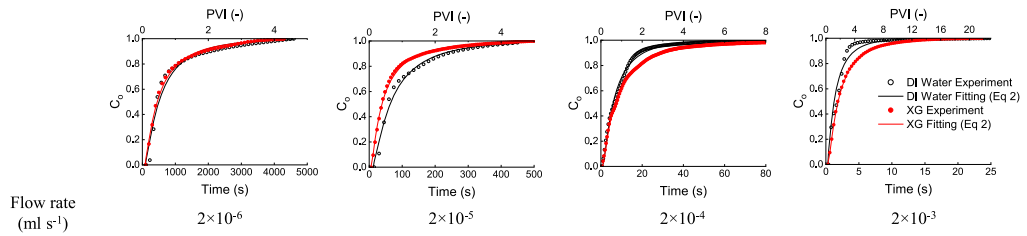


FIG. 4. Concentration breakthrough curves (data points) and the fitted results (solid red lines) using Eq. (2) for DI water and XG solutions for several injection rates, where the bottom x axis represents time, top x axis represents pore volume injected (PVI), and the y axis C_o represent the average effluent concentration.

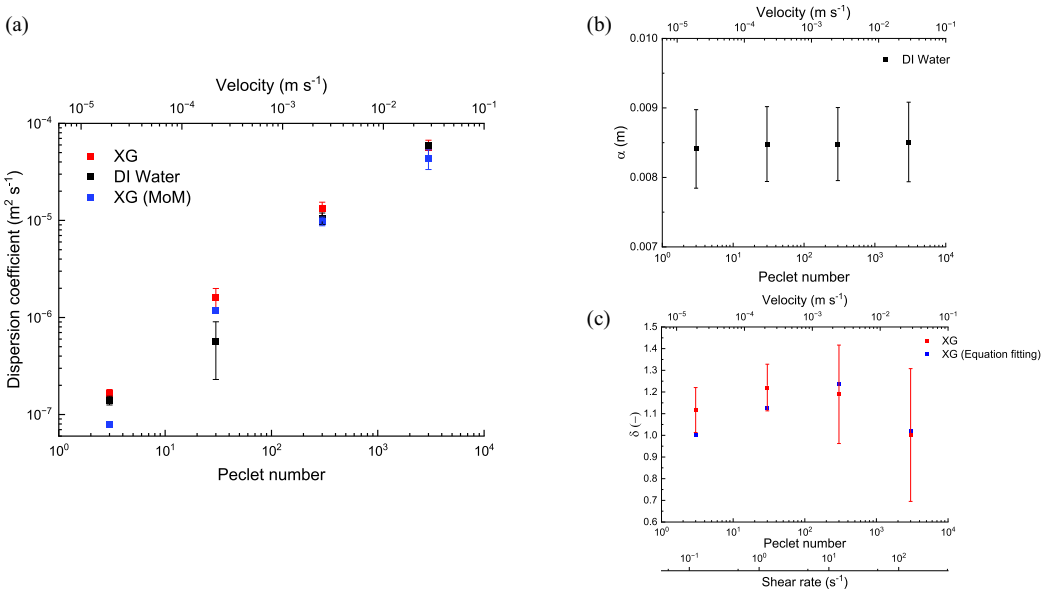


FIG. 5. (a) Fitted average dispersion coefficient for DI water and XG solution across all the experiments versus *Pe* and injected velocity. The red squares represent the fitting for XG from the Ogata-Banks equation, and the blue squares represent the fitting for XG from MoM. Error bars represent standard deviations calculated from 1 to 3 of repeated experiments, (b) dispersivity of the micromodel using the transport in the DI water solution, and (c) Non-Newtonian correction factor calculated using the transport in XG solution as a function of *Pe* and injected velocity, blue square color represents the fitting for XG using Eq. (18).

equivalently, $D_L/D = \alpha \mathrm{Pe}^{\beta}$, has been used to correlate the experimental data. β is often assumed to be 1, particularly in theoretical modeling, although many experiments indicate that $\beta \approx 1.15$–1.3 [44]. Assuming that the dispersion coefficient and velocity have a linear relationship, where $\beta = 1$, then α represents the dispersivity. Also, by calculating the slope of the dispersion vs the velocity in a log-log plot, β values for Xanthan gum ranged between 0.99–1.079.

3. Dispersivity for the non-Newtonian fluids

The dispersivity (α) represents a characteristic length scale [44–46] and is generally considered to be a function of the morphology of porous media [44,45], defined as $\alpha = D_L/v$. Our experimental data show that even in our non-Newtonian experiments $\beta \approx 1$, which allows us to use the same definition for dispersivity. All previous studies have focused on solute transport in the flow of Newtonian fluids, where viscosity remains constant regardless of the hydrodynamics. Consequently, the dispersivities presented in such studies depend solely on the properties of the porous medium. To distinguish solute transport in Newtonian and non-Newtonian fluids, we introduce the influence of non-Newtonian fluid rheology on dispersivity in our following analysis.

Based on the method of moments, the dispersion coefficient can be defined as [47]

$$D_L = \frac{1}{2}\frac{d\sigma_x^2}{dt}, \quad \sigma_x^2 = \sum (x_i - \bar{x})^2 p(x_i). \tag{8}$$

Since $x_i = u_i t$, we can express it as

$$D_L = \sigma_u^2 t, \tag{9}$$

where σ_x^2 and σ_u^2 represent the variances of x and u, respectively.

Under the fully mixed conditions, dispersivity α is defined as $\alpha = D_L/u$. Therefore, dispersivity can be expressed in terms of the velocity field variability relative to the mean velocity:

$$\alpha = \mathcal{L}\frac{\sigma_u^2}{u^2}, \tag{10}$$

where $\mathcal{L}$ denotes the characteristic length associated with velocity field variability.

There is no analytical solution in the literature for the effective shear rate in porous media for Carreau fluids. However, for a power-law fluid ($\eta = C\dot{\gamma}^{n-1}$), an expression has been proposed [48] that models the transition zone in the shear-thinning region as follows:

$$\dot{\gamma}_{\text{eff}} = \frac{C}{\sqrt{2}}\left(\frac{3n+1}{4n}\right)^{n/(n-1)}\frac{u}{\sqrt{k\phi}}, \tag{11}$$

where C, k, and ϕ represent a material constant, permeability, and Darcy velocity, respectively.

Substituting Eq. (11) into Eq. (7) and reformulating the expression in terms of u yields

$$u = \frac{\sqrt{2}}{\lambda C}\left(\frac{4n}{3n+1}\right)^{n/(n-1)}\sqrt{k\phi}\left(\tilde{\eta}^{\frac{2}{n-1}} - 1\right)^{1/2}. \tag{12}$$

Applying the Gauss propagation theorem (uncertainty propagation), we demonstrate that statistical variability in velocity u results from statistical variability in other effective variables. Using Eq. (12), we approximate the variance of u, σ_u^2, as

$$\sigma_u^2 \approx \left(\frac{\partial u}{\partial \eta}\right)^2\sigma_\eta^2 + \left(\frac{\partial u}{\partial k}\right)^2\sigma_k^2. \tag{13}$$

Dividing σ_u^2 by u^2, and taking the derivatives using Eq. (12), we obtain

$$\frac{\sigma_u^2}{u^2} \approx \frac{\sigma_k^2}{4k^2} + \frac{\tilde{\eta}^{\frac{4}{n-1}}\sigma_{\tilde{\eta}}^2}{\tilde{\eta}^2\left(\tilde{\eta}^{\frac{2}{n-1}} - 1\right)^2(n-1)^2}, \tag{14}$$

which simplifies to

$$\frac{\sigma_u^2}{u^2} \approx \frac{\sigma_k^2}{4k^2}\left(1 + \frac{\tilde{\eta}^{\frac{4}{n-1}}}{\left(\tilde{\eta}^{\frac{2}{n-1}} - 1\right)^2(n-1)^2}\frac{\frac{\sigma_{\tilde{\eta}}^2}{\tilde{\eta}^2}}{\frac{\sigma_k^2}{4k^2}}\right). \tag{15}$$

Assuming small variations in $\tilde{\eta}$ and $\dot{\gamma}$, we approximate $\sigma_x \approx \partial x$. The final expression is

$$\frac{\sigma_u^2}{u^2} \approx \frac{\sigma_k^2}{4k^2}\left(1 + \frac{\tilde{\eta}^{\frac{4}{n-1}}}{\left(\tilde{\eta}^{\frac{2}{n-1}} - 1\right)^2(n-1)^2}\left(\frac{\partial \ln \tilde{\eta}}{\partial \ln \dot{\gamma}}\right)^2\right). \tag{16}$$

Finally, combining Eqs. (10) and (16), dispersivity can be defined as

$$\alpha \approx \mathcal{L}\frac{\sigma_k^2}{4k^2}\underbrace{\left(1 + \frac{\tilde{\eta}^{\frac{4}{n-1}}}{\left(\tilde{\eta}^{\frac{2}{n-1}} - 1\right)^2(n-1)^2}\left(\frac{\partial \ln \tilde{\eta}}{\partial \ln \dot{\gamma}}\right)^2\right)}_{\delta}. \tag{17}$$

The correction factor of dispersivity, δ, in Eq. (17) accounts for the influence of non-Newtonian fluid rheology on dispersivity. In the existing literature, where all previous experimental studies focus on Newtonian fluids, the second term in δ is zero. Consequently, δ depended solely on the permeability field and its variation in those studies.

TABLE I. The Newtonian fluid fitted parameters resulted from Eq. (2) based on DI water experimental average effluent concentration results.

Flow rate (ml s^{-1})	Dispersion coefficient (m^2 s^{-1})	Fitted velocity (m s^{-1})	Dispersivity (m)	MSE (-)	RMSE (-)
2×10^{-3}	5.95×10^{-5}	7.00×10^{-3}	8.51×10^{-3}	3.36×10^{-3}	5.62×10^{-2}
2×10^{-4}	1.05×10^{-5}	1.24×10^{-3}	8.48×10^{-3}	5.49×10^{-4}	2.27×10^{-2}
2×10^{-5}	7.83×10^{-7}	9.22×10^{-5}	8.48×10^{-3}	1.08×10^{-3}	3.23×10^{-2}
2×10^{-6}	1.44×10^{-7}	1.71×10^{-5}	8.41×10^{-3}	1.20×10^{-3}	3.44×10^{-2}

Due to simplifications and approximations made during the derivation, we introduced two fitting parameters, a_1 and a_2, which have been used to fit the experimental data. Thus, we obtain

$$\alpha = \mathcal{L}\frac{\sigma_k^2}{4k^2}\underbrace{\left(1 + \frac{\tilde{\eta}^{2a_1}}{a_2(\tilde{\eta}^{a_1} - 1)^2}\left(\frac{\partial \ln \tilde{\eta}}{\partial \ln \dot{\gamma}}\right)^2\right)}_{\delta}. \tag{18}$$

To examine the functionality of the correction factor δ in relation to flow rate within the experimental data, first, the dispersivity of the tracer in the DI water solution was measured, as shown in Figs. 5(b) and 5(c). Subsequently, the non-Newtonian correction factor, δ, was calculated for solute transport in the XG solution. At the highest flow rate, $\delta \approx 1$, indicating that the spatial variability of pore-scale fluid velocity, which drives hydrodynamic dispersion, closely resembles that of water. This confirms that non-Newtonian fluids exhibit nearly Newtonian behavior at high velocities in these experiments.

The dynamic behavior of non-Newtonian fluids within the pore space, along with the corresponding solute transport, undergoes significant changes as the injection flow rate increases. This transformation is clearly illustrated in Fig. 3, which shows a uniform solute displacement pattern at low injection rates. The uniformity strongly suggests that diffusion is the dominant mechanism governing solute transport in this regime, with its efficiency and pattern remaining largely unaffected by changes in velocity, as corroborated by Fried and Combarnous [49]. This observation is crucial for understanding fluid dynamics in various contexts in which non-Newtonian fluids are involved. When the injection rate of non-Newtonian fluids increases, their viscosity decreases, which fundamentally alters their behavior and the way they transports a solute.

Additionally, at intermediate flow rates, solute transport is significantly influenced by the fluid's rheology, marking a distinct transition in solute transport characteristics. From the data in Fig. 5(a), it is evident that as the viscosity of the non-Newtonian fluid decreases due to shear thinning, the fluid velocity increases, leading to an increase in the dispersion coefficient. When the injection flow rate is substantially elevated, the behavior of the non-Newtonian fluid approaches that of a Newtonian fluid, as seen in Fig. 5(c), due to the presence of a plateau region where viscosity becomes independent of shear rate; see Fig. 3. This shift in fluid dynamics is supported by previous studies [15,50–52]. Due to experimental limitations, we were only able to test a restricted number of flow rates. Consequently, the number of data points is limited, and those indicated by error bars may appear large or overlapping, particularly at low and high Péclet numbers. Please note for the low and high Péclet numbers, overlapping of the dispersivity or dispersion coefficient for the Newtonian and non-Newtonian fluids is consistent with the theoretical expectations reported in [15]. The range of error bars is consistent and even smaller than the reported error bars in former experiments such as [53].

Tables I and II present the dispersion coefficients, dispersivity, and the non-Newtonian correction factor. The root mean square error (RMSE) and the mean square error (MSE) were used to quantify the difference between the fitted and actual experimental data for the average effluent concentration. To better understand the differences between the evolution of solute transport instabilities in

TABLE II. The non-Newtonian fluid fitted parameters resulted from Eq. (2) based on Xanthan gum experimental average effluent concentration results.

Flow rate (ml s^{-1})	Dispersioncoefficient (m^2 s^{-1})	Fitted velocity (m s^{-1})	Non-Newtonian correct factor (-)	MSE (-)	RMSE (-)
2×10^{-3}	5.62×10^{-5}	6.55×10^{-3}	1.00	5.02×10^{-4}	2.08×10^{-2}
2×10^{-4}	1.32×10^{-5}	1.20×10^{-3}	1.19	2.51×10^{-4}	1.46×10^{-2}
2×10^{-5}	1.61×10^{-6}	1.60×10^{-4}	1.22	5.34×10^{-5}	7.08×10^{-3}
2×10^{-6}	1.64×10^{-7}	1.64×10^{-5}	1.12	2.43×10^{-4}	1.56×10^{-2}

Newtonian and non-Newtonian fluids, the fractal dimension of the area occupied by the solute at the breakthrough point was calculated using the box-counting method [54,55]. The results are shown in Fig. 6, which indicates that the fractal dimension decreases with increasing the flow rate [18]. More importantly, however, is that the fractal dimension in the shear-thinning fluid is smaller than that in the Newtonian one, implying thinner but more frequent fingers, which is in agreement with the results presented in Fig. 3 and the discussions above.

IV. CONCLUSION

This study presents experimental research and corresponding analysis using optical microscopy to delineate the dispersion of a solute within a Xanthan gum solution, a shear-thinning fluid, compared to dispersion in water as the Newtonian fluid. The porous domain is a transparent glass micromodel with random features of pore morphology. Experiments were performed in four different flow rates, representing four different Péclet numbers and solute transport within the transport micromodel was visualized and analyzed to estimate the transport properties (dispersion coefficient and dispersivity) at each flow rate. This experimental research demonstrates that transport in shear-thinning fluid flow through porous media is enhanced compared to Newtonian fluids. Furthermore, it highlights that the conventional definition of dispersivity does not hold for non-Newtonian fluids. Due to the shear dependence of viscosity, the spatial velocity field alters with injection flow rate for shear-thinning fluids, resulting in a nonmonotonic relation between dispersivity and flow rate compared to Newtonian fluids. We have also shown through theoretical analysis that a correction factor, which depends on the fluids' rheology, is needed to assess the effect of fluid properties on dispersivity accurately. The experimental results confirm that the non-Newtonian fluid behaves as a Newtonian fluid at very high *Pe* numbers in terms of dispersion coefficient, as evidenced by the similarity between the dispersion coefficients of the non-Newtonian and Newtonian fluids.

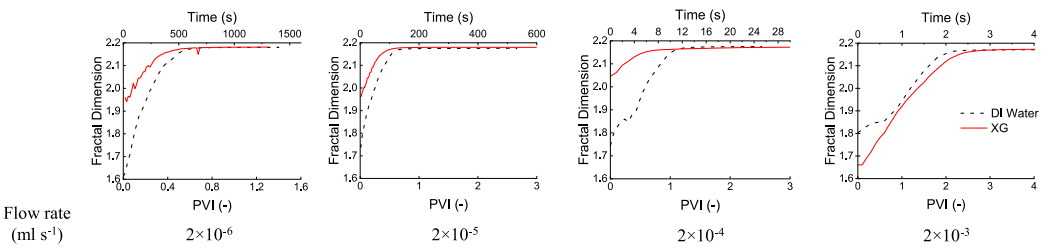


FIG. 6. Evolution of the fractal dimension of the concentration map for Newtonian and non-Newtonian fluids until the breakthrough time.

ACKNOWLEDGMENTS

The author A.A.-Q. acknowledges Kuwait Petroleum Corporation and Kuwait Oil Company for the scholarship for Ph.D. studies at the University of Manchester. M.S. is grateful to the United States National Science Foundations for partial support of his work under Grant CBET 2000966.

A.A.-Q.: investigation, methodology, data curation, formal analysis, resources, writing—original draft; J.S.: training, methodology, data curation, formal analysis, supervision, writing—original draft; T.S.: discussion; M.S.: discussion, quality assessment; V.N.: project design, supervision, methodology, resources, validation, formal analysis, quality assessment, conceptualization, writing—review and editing. All authors contributed to writing the final manuscript and proof reading.

The authors have no conflicts to disclose.

DATA AVAILABILITY

The data that support the findings of this study are available from the corresponding author upon reasonable request.

[1] R. B. Bird, R. C. Armstrong, and O. Hassager, Dynamics of polymeric liquids, in *Fluid Mechanics*, 2nd ed. (Wiley, New York, 1987), Vol. 1.

[2] G. R. Sanderson, Applications of Xanthan gum, Brit. Poly. J. **13**, 71 (1981).

[3] E. Blanco, H. Shen, and M. Ferrari, Principles of nanoparticle design for overcoming biological barriers to drug delivery, Nat. Biotechnol. **33**, 941 (2015).

[4] F. Gentile, M. Ferrari, and P. Decuzzi, The transport of nanoparticles in blood vessels: The effect of vessel permeability and blood rheology, Ann. Biomed. Eng. **36**, 254 (2008).

[5] D. Bolster, M. Dentz, and T. Le Borgne, Solute dispersion in channels with periodically varying apertures, Phys. Fluids **21**, 056601 (2009).

[6] D. Diaz, C. Somaruga, C. Norman, and J. Romero, Colloidal dispersion gels improve oil recovery in a heterogeneous Argentina waterflood, in *SPE Improved Oil Recovery Conference* (SPE, Tulsa, Oklahoma, 2008), p. SPE–113320.

[7] J. Savins, Non-Newtonian flow through porous media, Ind. Eng. Chem. **61**, 18 (1969).

[8] L. M. Amoo and R. L. Fagbenle, Overview of non-Newtonian boundary layer flows and heat transfer, in *Applications of Heat, Mass and Fluid Boundary Layers* (Woodhead Publishing, 2020), pp. 413–435.

[9] M. Sahimi, Nonlinear transport processes in disordered media, AIChE J. **39**, 369 (1993).

[10] B. Berkowitz, Characterizing flow and transport in fractured geological media: A review, Adv. Water Resour. **25**, 861 (2002).

[11] Y. Chen, H. Steeb, H. Erfani, N. K. Karadimitriou, M. S. Walczak, M. Ruf, D. Lee, S. An, S. Hasan, T. Connolley *et al.*, Nonuniqueness of hydrodynamic dispersion revealed using fast 4D synchrotron x-ray imaging, Sci. Adv. **7**, eabj0960 (2021).

[12] F. Zami-Pierre, R. De Loubens, M. Quintard, and Y. Davit, Polymer flow through porous media: Numerical prediction of the contribution of slip to the apparent viscosity, Transp. Porous Media **119**, 521 (2017).

[13] V. Chaplain, P. Mills, G. Guiffant, and P. Cerasi, Model for the flow of a yield fluid through a porous medium, J. Phys. II France **2**, 2145 (1992).

[14] A. D'Onofrio, V. Freytes, M. Rosen, C. Allain, and J. Hulin, Echo tracer dispersion in flows of polymer solutions through porous media: A tool for detecting weak permeability heterogeneities? Eur. Phys. J. E **7**, 251 (2002).

[15] S. An, M. Sahimi, and V. Niasar, Upscaling hydrodynamic dispersion in non-Newtonian fluid flow through porous media, Water Resour. Res. **58**, e2022WR032238 (2022).

[16] J. Pearson and P. Tardy, Models for flow of non-Newtonian and complex fluids through porous media, J. Non-Newtonian Fluid Mech. **102**, 447 (2002).
[17] T. Sochi, Flow of non-Newtonian fluids in porous media, J. Polym. Sci. Part B: Polym. Phys. **48**, 2437 (2010).
[18] S. An, M. Sahimi, T. Shende, M. Babaei, and V. Niasar, Enhanced thermal fingering in a shear-thinning fluid flow through porous media: Dynamic pore network modeling, Phys. Fluids **34**, 023105 (2022).
[19] S. De, P. Krishnan, J. van der Schaaf, J. Kuipers, E. Peters, and J. Padding, Viscoelastic effects on residual oil distribution in flows through pillared microchannels, J. Colloid Interface Sci. **510**, 262 (2018).
[20] C. A. Browne, A. Shih, and S. S. Datta, Pore-scale flow characterization of polymer solutions in microfluidic porous media, Small **16**, 1903944 (2020).
[21] A. Paterson, A. d'Onofrio, C. Allain, J. Hulin, M. Rosen, and C. Gauthier, Tracer dispersion in a polymer solution flowing through a double porosity porous medium, J. Phys. II France **6**, 1639 (1996).
[22] A. D'onofrio, A. Paterson, C. Allain, J. Hulin, and M. Rosen, Flow of shear thinning polymer solutions in heterogeneous porous media: Tracer dispersion measurements, Rev. Inst. Fr. Pét. **52**, 219 (1997).
[23] B. D. Hughes and M. Sahimi, Diffusion in disordered systems with multiple families of transport paths, Phys. Rev. Lett. **70**, 2581 (1993).
[24] B. D. Hughes and M. Sahimi, Stochastic transport in heterogeneous media with multiple families of transport paths, Phys. Rev. E **48**, 2776 (1993).
[25] C. A. Browne, R. B. Huang, C. W. Zheng, and S. S. Datta, Homogenizing fluid transport in stratified porous media using an elastic flow instability, J. Fluid Mech. **963**, A30 (2023).
[26] M. Dejam, Dispersion in non-Newtonian fluid flows in a conduit with porous walls, Chem. Eng. Sci. **189**, 296 (2018).
[27] D. Reinoso, M. Martín-Alfonso, P. Luckham, and F. Martínez-Boza, Rheological characterisation of xanthan gum in brine solutions at high temperature, Carbohydr. Polym. **203**, 103 (2019).
[28] N. Karadimitriou, M. Musterd, P. Kleingeld, M. Kreutzer, S. Hassanizadeh, and V. Joekar-Niasar, On the fabrication of PDMS micromodels by rapid prototyping, and their use in two-phase flow studies, Water Resour. Res. **49**, 2056 (2013).
[29] J. Shokri, O. E. Godinez-Brizuela, H. Erfani, Y. Chen, M. Babaei, B. Berkowitz, and V. Niasar, Impact of displacement direction relative to heterogeneity on averaged capillary pressure-saturation curves, Water Resour. Res. **58**, e2021WR030748 (2022).
[30] S. S. Datta, A. M. Ardekani, P. E. Arratia, A. N. Beris, I. Bischofberger, G. H. McKinley, J. G. Eggers, J. E. López-Aguilar, S. M. Fielding, A. Frishman *et al.*, Perspectives on viscoelastic flow instabilities and elastic turbulence, Phys. Rev. Fluids **7**, 080701 (2022).
[31] N. K. Karadimitriou, V. Joekar-Niasar, M. Babaei, and C. A. Shore, Critical role of the immobile zone in non-Fickian two-phase transport: A new paradigm, Environ. Sci. Technol. **50**, 4384 (2016).
[32] A. Ogata and R. B. Banks, *A Solution of the Differential Equation of Longitudinal Dispersion in Porous Media* (US Government Printing Office, 1961).
[33] M. N. Goltz and P. V. Roberts, Using the method of moments to analyze three-dimensional diffusion-limited solute transport from temporal and spatial perspectives, Water Resour. Res. **23**, 1575 (1987).
[34] B. J. Wagner and S. M. Gorelick, A statistical methodology for estimating transport parameters: Theory and applications to one-dimensional advectivec-dispersive systems, Water Resour. Res. **22**, 1303 (1986).
[35] C. C. Frippiat and A. E. Holeyman, A comparative review of upscaling methods for solute transport in heterogeneous porous media, J. Hydrol. X **362**, 150 (2008).
[36] Y. Gong and M. Piri, Pore-to-core upscaling of solute transport under steady-state two-phase flow conditions using dynamic pore network modeling approach, Transp. Porous Media **135**, 181 (2020).
[37] F. J. Leij and N. Toride, Discrete time-and length-averaged solutions of the advection-dispersion equation, Water Resour. Res. **31**, 1713 (1995).
[38] C. Yu, A. Warrick, and M. Conklin, A moment method for analyzing breakthrough curves of step inputs, Water Resour. Res. **35**, 3567 (1999).
[39] M. M. Mrokowska and A. Krztoń-Maziopa, Viscoelastic and shear-thinning effects of aqueous exopolymer solution on disk and sphere settling, Sci. Rep. **9**, 7897 (2019).

[40] R. Speers and M. Tung, Concentration and temperature dependence of flow behavior of xanthan gum dispersions, J. Food Sci. **51**, 96 (1986).
[41] D. M. Meter and R. B. Bird, Tube flow of non-Newtonian polymer solutions: Part I. Laminar flow and rheological models, AIChE J. **10**, 878 (1964).
[42] T. Shende, V. J. Niasar, and M. Babaei, Effective viscosity and Reynolds number of non-Newtonian fluids using meter model, Rheol. Acta **60**, 11 (2021).
[43] A. Lodge and J. Meissner, On the use of instantaneous strains, superposed on shear and elongational flows of polymeric liquids, to test the Gaussian network hypothesis and to estimate the segment concentration and its variation during flow, Rheol. Acta **11**, 351 (1972).
[44] M. Sahimi, *Flow and Transport in Porous Media and Fractured Rock: From Classical Methods to Modern Approaches* (John Wiley & Sons, Weinheim, Germany, 2011).
[45] J. Bear, On the tensor form of dispersion in porous media, J. Geophys. Res. **66**, 1185 (1961).
[46] A. E. Scheidegger, General theory of dispersion in porous media, J. Geophys. Res. **66**, 3273 (1961).
[47] N. G. Barton, On the method of moments for solute dispersion, J. Fluid Mech. **126**, 205 (1983).
[48] W. J. Cannella, C. Huh, and R. S. Seright, Prediction of xanthan rheology in porous media, in *SPE Annual Technical Conference and Exhibition* (SPE, Houston, Texas, 1988), p. SPE-18089-MS.
[49] J. Fried and M. Combarnous, Dispersion in porous media, in *Advances in Hydroscience*, edited by V. T. Chow, Advances in Hydroscience Vol. 7 (Elsevier, New York, 1971), pp. 169–282.
[50] M. Sahimi, Mixing and dispersion in flow through porous media, in *Applications of Percolation Theory* (Springer, 2023), pp. 155–174.
[51] R. P. Chhabra, Non-Newtonian fluids: An introduction, in *Rheology of Complex Fluids* (Springer, New York, 2010), pp. 3–34.
[52] T. Sochi, Non-Newtonian flow in porous media, Polymer **51**, 5007 (2010).
[53] B. Bijeljic and M. Blunt, Pore-scale modeling and continuous random walk analysis of dispersion in porous media, Water Resour. Res. **42**, W01202 (2006).
[54] K. Foroutan-pour, P. Dutilleul, and D. Smith, Advances in the implementation of the box-counting method of fractal dimension estimation, Appl. Math. Comput. **105**, 195 (1999).
[55] J. Li, Q. Du, and C. Sun, An improved box-counting method for image fractal dimension estimation, Pattern Recognit. **42**, 2460 (2009).